

1 **Coastal polynyas enable transitions between high and**
2 **low West Antarctic ice shelf melt rates**

3 **Ruth Moorman¹, Andrew F. Thompson¹, and Earle A. Wilson²**

4 ¹Environmental Science and Engineering, California Institute of Technology, Pasadena, California, USA

5 ²Department of Earth System Science, Stanford University, Stanford, California, USA

6 **Key Points:**

- 7 • Rates of ocean-driven Amundsen Sea ice shelf melt respond to variations in warm
8 water transport to the coast and modification at the coast.
9 • A simple Amundsen Sea continental shelf overturning model, based on water mass
10 transformation, reveals bistable high and low melt regimes.
11 • Feedbacks between glacial melt and polynya convection are central to the bista-
12 bility and produce variability consistent with observations.

Corresponding author: Ruth Moorman, rmoorman@caltech.edu

Abstract

Melt rates of West Antarctic ice shelves in the Amundsen Sea track large decadal variations in the volume of warm water at their outlets. This variability is generally attributed to wind-driven variations in warm water transport towards ice shelves. Inspired by conceptual representations of the global overturning circulation, we introduce a simple model for the evolution of the thermocline, which caps the warm water layer at the ice-shelf front. This model demonstrates that interannual variations in coastal polynya buoyancy forcing can generate large decadal-scale thermocline depth variations, even when the supply of warm water from the shelf-break is fixed. The modeled variability involves transitions between bistable high and low melt regimes, enabled by feedbacks between basal melt rates and ice front stratification strength. Our simple model captures observed variations in near-coast thermocline depth and stratification strength, and poses an alternative mechanism for warm water volume changes to wind-driven theories.

Plain Language Summary

Ice loss from the West Antarctic Ice Sheet contributes significantly to current and projected rates of global sea-level rise. The ice sheet is primarily losing mass via glaciers that flow from the Antarctic continent into the Amundsen Sea, where floating ice shelves are exposed to much warmer ocean waters than elsewhere around Antarctica. In this work we present a simplified mathematical model for the volume of warm water at Amundsen Sea ice shelf fronts that reproduces observed patterns of warm water variability. The modeled variability relies on interactions between ice shelf melt and coastal polynyas, regions where enhanced wintertime sea-ice production can trigger mixing that diverts heat carried by warm waters away from the ice shelf and into the atmosphere. Higher melt rates inhibit polynya convection, allowing more warm water into the ice shelf cavity and reinforcing a high melt state, whilst lower melt rates facilitate polynya convection, diverting heat away from the ice shelf and reinforcing a low melt state. Interannual variations in polynya sea-ice production trigger shifts between these reinforcing states. Our results promote the importance of coastal processes in explaining observed variations in Amundsen Sea ice shelf melt, which have previously been attributed to remote wind patterns.

1 Introduction

Recorded mass loss from the West Antarctic Ice Sheet (WAIS) has been driven by the accelerating flow of ice streams that terminate at rapidly thinning ice shelves in the Amundsen Sea embayment (Mouginot et al., 2014; Paolo et al., 2015; IMBIE Team, 2018). Whilst ice shelf thinning does not directly impact the ice sheet mass balance, the restraining or “buttressing” effect of floating ice shelves on upstream grounded ice flow is critical for limiting ice discharge through glaciers (Fürst et al., 2016; Morlighem et al., 2020). The observed thinning of buttressing ice shelves in the Amundsen Sea has been associated with high rates of basal melt driven by modified Circumpolar Deep Water (mCDW) (Adusumilli et al., 2020; Pritchard et al., 2012; Shepherd et al., 2004; Turner et al., 2017); a warm (2-4°C above freezing) water mass that floods the lower layers of the West Antarctic continental shelf and carries heat from the open ocean to ice shelf cavities via glacially-carved troughs (Walker et al., 2007; Dutrieux et al., 2014). Future projections of the WAIS require accurate representation of forcings that dictate the access of warm mCDW to Amundsen Sea ice shelf cavities.

Hydrographic observations from the Amundsen Sea embayment reveal decadal variations in the thickness of the mCDW layer (Dutrieux et al., 2014; Jenkins et al., 2018) that overwhelm multidecadal ocean warming trends previously considered the driver of ice shelf thinning (Schmidtke et al., 2014). This decadal variability is well observed in front of the Dotson Ice Shelf, where sea-ice free conditions in the Amundsen Sea Polynya

(ASP) permit the collection of summertime hydrographic profiles near the ice shelf front (Figure 1). Observations from 2000 to 2018 reveal high amplitude (~ 400 m), low frequency (~ 10 year period) variability in the thermocline depth, characterized by a warm phase with thick mCDW from 2006-2011 followed by a cool phase with thin mCDW from 2012-2016 and a potential return to warm conditions in 2018 (Figure 1b,d) (Jenkins et al., 2018; Kim et al., 2021). The observed thermocline variability has been linked to Dotson Ice Shelf basal melt rates (Jenkins et al., 2018) and may be implicated in ice shelf thinning trends, either via historical warm phases triggering geometric grounding line retreat that continues to the present (Jenkins et al., 2016) or via a trend in the frequency of warm phases unresolved by the short observational record (Naughten et al., 2022).

This mCDW thickness variability is often attributed to mechanical wind forcing. Numerous studies relate eastward wind anomalies over the Amundsen shelf with warm phases, suggesting these winds enhance poleward mCDW transport by barotropically accelerating the Amundsen undercurrent (Assmann et al., 2013; Dotto et al., 2019, 2020; Holland et al., 2019; Naughten et al., 2022). Recently, Silvano et al. (2022) affirm this barotropic mechanism at short timescales, but find eastward winds have the opposite effect on poleward mCDW transport at decadal (and longer) timescales due to baroclinic adjustment of the undercurrent. Melt rate variability is more consistent with these longer time scales. Variations in coastal (Yang et al., 2022), shelf-break (Kim et al., 2017; Weber et al., 2019), and shelf integrated (Kim et al., 2021) wind-driven Ekman pumping are also suggested as potential drivers. Though mechanisms differ, these studies consistently present wind-driven variability of shoreward mCDW transport as the driver of thermocline depth variability and associated melt variability in the Amundsen Sea.

There are indications that the wind-driven framework is incomplete. Coastal thermocline depth and heat content variability is substantially amplified relative to the shelf-break in both observations and simulations (e.g. Kim et al., 2021; Silvano et al., 2022; Naughten et al., 2022), a feature not directly addressed by wind-driven mechanisms. Further, while thermocline displacements predicted from winds correlate well with observations, they underestimate the amplitude of coastal signals (Kim et al., 2021). Prompted by this amplitude gap, we revisit the Dotson Ice Front hydrography. Years with thick mCDW layers (2006-2011) are consistently associated with stronger stratification (Figure 1d) and more buoyant, meltwater modified Winter Waters (WW) relative to years with thin mCDW layers (2000, 2012-2016). Further, during warm years, modification by glacial meltwater pulls WW, a remnant of the preceding winter’s sea-ice modified mixed layer, away from the freezing line and towards the mCDW-meltwater mixing line (the “Gade Line”) (Figure 1c). These hydrographic properties suggest a role for water mass transformation by sea-ice, produced in large quantities in coastal polynyas generally and the ASP in particular (Macdonald et al., 2023; Tamura et al., 2008, 2016), and glacial ice in the observed variability.

Informed by a high-resolution regional ocean simulation and the observations presented above, we introduce a simple overturning circulation model that represents the transformation of mCDW into cool thermocline waters both within the Dotson Ice Shelf cavity and at its entrance in the ASP. Using this model, we demonstrate that variations in polynya surface buoyancy fluxes, directly related to net local sea-ice formation rates, can generate large decadal scale thermocline depth variations in the absence of variable shelf-break forcing, posing an alternative mechanism for observed variability. The modeled thermocline variability takes the form of transitions between bistable warm and cool regimes, made possible by feedbacks between basal ice melt and stratification at the ice front. With this work, we underscore that variations in mCDW consumption, in addition to mCDW supply, can strongly influence the exposure of West Antarctic ice shelves to ocean heat. This work uses the Dotson Ice Shelf as a case study, however our model is applicable to other West Antarctic ice shelves fringed by coastal polynyas, including Venable and Pine Island ice shelves.

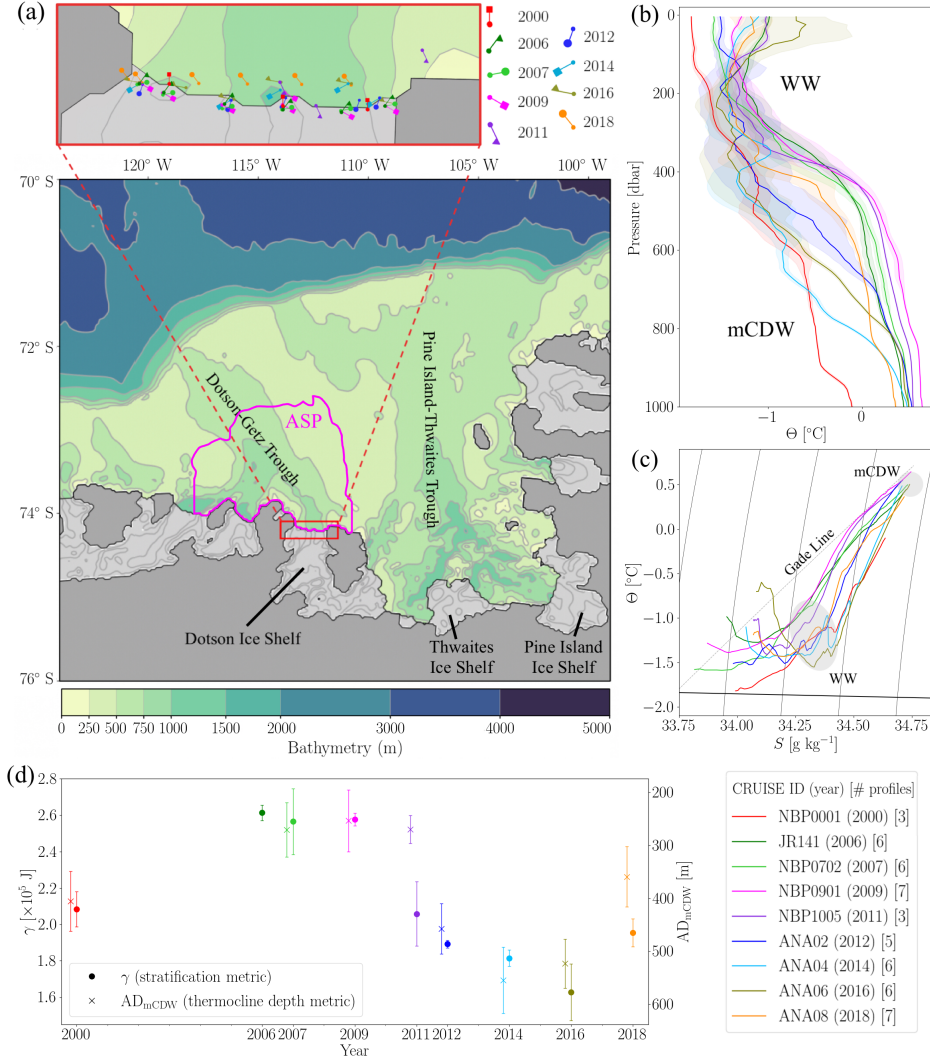


Figure 1. (a) Map of the Amundsen Sea embayment showing open ocean bathymetry (green shading; grey contours), ice shelf cavity bathymetry (grey shading; grey contours), and the grounded ice zone (dark grey). The Dotson Ice Front is outlined in red with an enlarged view provided above. The January climatological mean (2004-2022) extent of the Amundsen Sea Polynya (ASP) is indicated by the pink contour (using Fetterer & Stewart., 2020). Locations of shipborne observations used to produce (b)-(d) are indicated in the enlarged map. (b,c) Cruise mean conservative temperature (Θ) profiles as a function of pressure (b) and absolute salinity (S) (c). Mean profiles (solid lines) and standard deviations (shading) are calculated in density space and sorted into pressure space (as in Dutrieux et al., 2014) before being smoothed with a 5 dbar rolling mean. Water masses discussed in the main text (modified Circumpolar Deep Water, mCDW, and Winter Water, WW) are labelled. Potential density (black contours), the freezing line (thick black line), and an example Gade line indicative of mixing between mCDW and glacial meltwater (dashed black line) are shown for reference in (c). (d) Timeseries of γ , a bulk indicator of stratification strength calculated as the potential energy required to homogenize profiles between 5 and 750 dbars (circles), and the absolute depth of the mCDW layer AD_{mCDW} , a proxy for the thermocline depth developed by Kim et al. (2021) (crosses) (details in Supporting Information S1). AD_{mCDW} and γ values are offset on the time axis for clarity. Variables required for the calculation of AD_{mCDW} were not obtained for 2006. Observations were collected in the austral summer between December (previous year) and March (listed year).

2 Methods

2.1 Ice front overturning model

Motivated by observational evidence that the ice front thermocline depth is tied to basal melt rates (Jenkins et al., 2018) and that barotropic heat transport is blocked at the ice shelf front (Wåhlin et al., 2020), we present a purely baroclinic model for heat transport to ice shelves reminiscent of simple models for the global overturning (Walin, 1982; Gnanadesikan, 1999). This baroclinic model represents the shoreward transport of warm mCDW and export of cool surface water masses, including WW and glacially modified CDW, within Amundsen Sea glacially carved troughs (e.g. Webber et al., 2019). This exchange is facilitated by water mass transformation, which may occur within the ice shelf cavity or the ASP. Transformations are modeled in a small region proximate to the ice shelf front, isolating the effect of coastal forcing from shelf-break processes.

Key model components are illustrated in Figure 2. Warm mCDW and overlying thermocline waters are represented as boxes within the small region where wintertime coastal polynya sea-ice formation is concentrated (50 km meridional, 55 km zonal extent to match the width of the Dotson Ice Shelf). The inflow of warm mCDW, Ψ_{in} , is prescribed to represent remote wind-driven variations in shoreward mCDW transport. This mCDW then transforms into offshore flowing thermocline waters via two pathways: by melting glacial ice and mixing with the resultant meltwater in the ice shelf cavity (Ψ_{ice}) or by mixing with overlying waters (Ψ_{P}) (Figure 2a,b). Assuming negligible volume input from meltwater, the steady state transports balance,

$$\Psi_{\text{in}} = \Psi_{\text{ice}} + \Psi_{\text{P}}. \quad (1)$$

The partitioning of mCDW transformation into Ψ_{ice} and Ψ_{P} is set by the thickness and relative buoyancy (i.e. stratification) of the mCDW and surface boxes. As illustrated in Figure 2c, the thermocline depth (h) and the thickness of the underlying mCDW layer (h_{mCDW}) evolve according to,

$$\frac{dh}{dt} = \frac{1}{L} [\Psi_{\text{ice}} + \Psi_{\text{P}} - \Psi_{\text{in}}], \quad (2)$$

$$h_{\text{mCDW}} = H - h, \quad (3)$$

where L is the meridional model extent and H is the ice front water column thickness (taken as 700 m). Ψ terms are converted from thickness fluxes to volume transports (1 Sv = $10^6 \text{ m}^3 \text{ s}^{-1}$) via the model zonal extent.

For the evolution of the stratification strength, we define buoyancy as the vertical acceleration a water mass experiences due to density perturbations, i.e. $b_i \equiv g\rho_i/\rho_0$. The buoyancy of the mCDW layer (b_{mCDW}) is kept constant, justified by the minimal variability in mCDW density in observations (Figure 1c). We set

$$b_{\text{mCDW}} = 0, \quad (4)$$

referencing our system to the buoyancy of the mCDW layer, such that the buoyancy differential between mCDW and thermocline waters, a metric for the ice front stratification strength, is $\Delta b = b - b_{\text{mCDW}} = b$ where b is the buoyancy of thermocline waters. The stratification strength (Δb) then evolves according to the divergence of buoyancy fluxes from the thermocline (Figure 2c),

$$\frac{d\Delta b}{dt} = \frac{1}{L} [(vb)_{\text{in}} - (vb)_{\text{out}}] + \frac{1}{h} [(wb)_{\text{in}} - (wb)_{\text{out}}] \quad (5)$$

where,

$$(vb)_{\text{in}} = \frac{\Psi_{\text{ice}} \Delta b_{\text{melt}}}{h}, \quad \text{and} \quad (6)$$

161
162

$$(vb)_{\text{out}} = \frac{\Psi_{\text{in}} \Delta b}{h}. \quad (7)$$

163 Here, Δb_{melt} is the buoyancy of waters transformed by mixing with glacial meltwater,
164 relative to b_{mCDW} , which we determine from hydrography to be $6.7 \times 10^{-3} \text{ m s}^{-2}$ (light-
165 est waters in Figure 1c). The vertical buoyancy budget comprises a prescribed surface
166 buoyancy flux due to net sea-ice formation,

$$(wb)_{\text{out}} = -F_{\text{surf}} \quad (8)$$

168 (negative F_{surf} values lower surface ocean buoyancy) and buoyancy loss to the under-
169 lying mCDW layer ($(wb)_{\text{in}}$). The latter simplifies to

$$(wb)_{\text{in}} = \frac{\Psi_{\text{P}} b_{\text{mCDW}}}{L} - \frac{\kappa_{\text{P}}(b - b_{\text{mCDW}})}{h} = -\frac{\kappa_{\text{P}} \Delta b}{h}. \quad (9)$$

171 given $b_{\text{mCDW}} = 0$. In (9) we select h as the most appropriate length-scale controlling
172 diffusive vertical buoyancy transfer, since a thicker surface layer poses greater resistance
173 to entrainment at its lower boundary when the primary energy source driving mixing
174 is input at the surface.

175 The form of the polynya diffusivity term in (9), κ_{P} , is central to the feedbacks de-
176 scribed in this study. Simply put, κ_{P} is a smoothed step function that transitions from

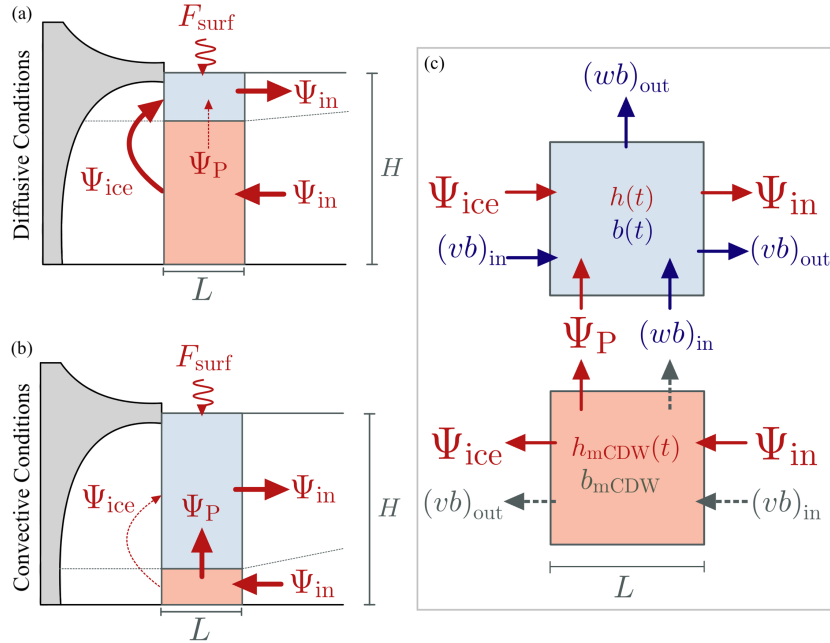


Figure 2. Schematic illustration of the ice front overturning model under (a) diffusive ($\kappa_{\text{P}} \rightarrow \kappa_{\text{diff}}$) and (b) convective ($\kappa_{\text{P}} \rightarrow \kappa_{\text{conv}}$) conditions. The thermocline and modified Circumpolar Deep Water (mCDW) layers are shaded blue and red respectively, and the ice shelf is shaded grey. Thick and dashed red arrows show the primary and secondary transformation pathways associated with each state. Thickness and buoyancy fluxes (Ψ_{in} , Ψ_{ice} , Ψ_{P} and F_{surf}) are indicated. (c) Schematic of the thickness and buoyancy budgets of the thermocline (upper; thickness and buoyancy evolved explicitly) and mCDW (lower; thickness evolved implicitly, buoyancy held constant) layers. The implied buoyancy budget of the mCDW layer is shown in grey, however b_{mCDW} does not evolve.

177 a small diffusive end member κ_{diff} when the thermocline is buoyant to a large convec-
 178 tive end member κ_{conv} when the thermocline approaches the density of the underlying
 179 mCDW. The effect is analogous to rapid transitions to vertical homogeneity triggered
 180 by static instability in simple models of open ocean polynyas (Martinson et al., 1981; Boot
 181 et al., 2021). Functionally, we define κ_{P} as,

$$182 \quad \kappa_{\text{P}}(\Delta b) = \frac{\kappa_{\text{conv}} - \kappa_{\text{diff}}}{2} \left(1 - \tanh(\phi(\Delta b - \Delta b_{\text{crit}})) \right) + \kappa_{\text{diff}}, \quad (10)$$

183 where κ_{conv} ($10^{-2} \text{ m}^2 \text{ s}^{-1}$) and κ_{diff} ($10^{-4} \text{ m}^2 \text{ s}^{-1}$, taken from Pine Island Ice Front ob-
 184 servations, Garabato et al., 2017) are vertical diffusivities, Δb_{crit} ($5 \times 10^{-4} \text{ m s}^{-2}$) is
 185 a small stratification strength at which turbulent convection onsets, and ϕ (5×10^4) is
 186 a parameter determining the steepness of the onset of convection. Our results are not
 187 sensitive to reasonable perturbations of the parameters.

188 The polynya mass transport term Ψ_{P} is obtained from (9) by assuming an advection-
 189 diffusion balance of buoyancy holds in the vertical (for details of similar parameteriza-
 190 tions see Marshall & Zanna, 2014; McDougall & Dewar, 1998; Munk, 1966),

$$191 \quad \Psi_{\text{P}} = -\frac{\kappa_{\text{P}} L}{h}. \quad (11)$$

192 Finally, the ice cavity overturning Ψ_{ice} is taken to be linearly proportional to mCDW
 193 thickness,

$$194 \quad \Psi_{\text{ice}} = \alpha h_{\text{mCDW}} = \alpha(H - h), \quad (12)$$

195 where α ($2.1 \times 10^{-3} \text{ m s}^{-1}$) is diagnosed from the WAIS 1080 regional simulation (see
 196 §2.2 and Supporting Information S2).

197 To summarize, the ice front overturning model is described by the following cou-
 198 pled differential equations for the thermocline depth (h) and stratification strength (Δb),

$$199 \quad \frac{dh}{dt} = \frac{1}{L} \left[\alpha(H - h) - \frac{\kappa_{\text{P}} L}{h} - \Psi_{\text{in}} \right], \quad (13)$$

$$200 \quad \frac{d\Delta b}{dt} = \frac{1}{Lh} \left[\alpha(H - h)\Delta b_{\text{melt}} - \Psi_{\text{in}}\Delta b \right] + \frac{1}{h^2} \left[F_{\text{surf}}h - \kappa_{\text{P}}\Delta b \right]. \quad (14)$$

201 All parameter values except κ_{P} are diagnosed from observations or WAIS 1080 (§2.2),
 202 and Ψ_{in} and F_{surf} are prescribed forcings representing the supply of mCDW (a remote
 203 forcing) and polynya surface buoyancy fluxes from sea-ice (a local forcing).
 204

205 **2.2 Regional general circulation model**

206 In addition to the ice front overturning model, we utilize monthly mean output from
 207 WAIS 1080, a high-resolution ($\sim 3 \text{ km}$ horizontal spacing) regional configuration of the
 208 Massachusetts Institute of Technology general circulation model (MITgcm) that repre-
 209 sents the Antarctic Peninsula to the western edge of the Amundsen Sea (Flexas et al.,
 210 2022). The model is forced at the surface by the European Centre for Medium-Range
 211 Weather Forecasts (ECMWF) reanalysis version 5 (ERA5; Hersbach et al., 2020) and
 212 integrated from 1992 to 2019. WAIS 1080 explicitly represents freezing and melting within
 213 ice shelf cavities of a fixed shape, making it suited to the study of ocean ice-shelf inter-
 214 actions at relatively short timescales. We use the control simulation from Flexas et al.
 215 (2022), who provide additional model details, to constrain the values of parameters (α)
 216 and forcings (F_{surf} , Ψ_{in}) of the ice front overturning model that are difficult to obtain
 217 directly from observations (details in Supporting Information S2).

218 **3 Results**

219 **3.1 Steady state model behavior**

220 Equilibrated solutions of the ice front overturning model map a hysteresis loop for
 221 the thermocline depth in response to varying surface buoyancy forcing (F_{surf}) when the

222 supply of mCDW from the shelf-break (Ψ_{in}) is held fixed (Figure 3a). Thus, warm and
 223 cold regimes can be realized with the same mCDW supply. This hysteresis loop is en-
 224 abled by a positive feedback between the depth of the ice front thermocline and the strat-
 225 ification of the ice front water column, the physics of which are parameterized in our ver-
 226 tical diffusivity term κ_{P} . A shallow ice front thermocline, equivalent to a thick mCDW
 227 layer, supports high melt rates within the cavity. The ensuing meltwater provides an ad-
 228 ditional buoyancy input to the thermocline that suppresses convection and reinforces the
 229 shallow thermocline position (upper “branch” of the hysteresis loop, Figure 3a). By con-
 230 trast, a deep ice front thermocline, equivalent to a thin mCDW layer, is associated with
 231 a weaker ice shelf melt rate and a reduced input of buoyant meltwater to the thermo-
 232 cline, comparatively preconditioning the water column for convection and reinforcing the
 233 deep thermocline position (lower “branch”, Figure 3a). This feedback produces bistable
 234 “diffusive” ($\kappa_{\text{P}} = \kappa_{\text{diff}}$, thick mCDW) and “convective” ($\kappa_{\text{P}} = \kappa_{\text{conv}}$, thin mCDW)
 235 steady states for a fixed supply of mCDW associated with a ~ 400 m thermocline depth
 236 differential. In this idealized model, most convective steady states are unstably strat-
 237 ified ($\Delta b < 0$) as they arise when strong negative buoyancy forcing is continuously ap-

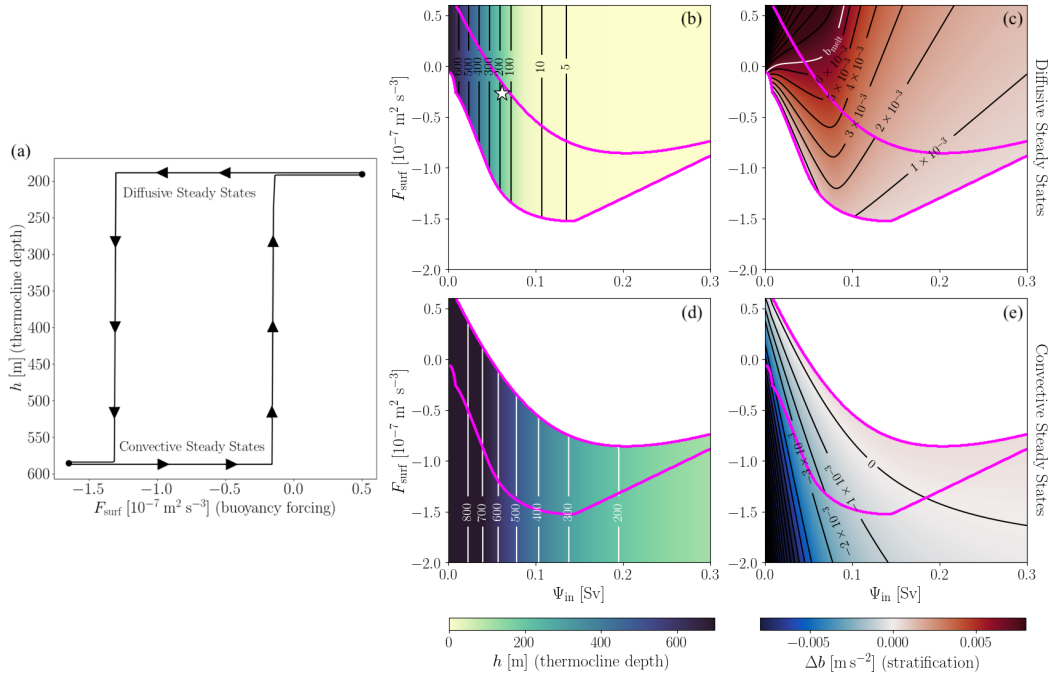


Figure 3. (a) Dependence of the model steady state on F_{surf} when Ψ_{in} is held fixed at the mean WAIS 1080 value (0.06 Sv). The model is evolved to steady state after incrementally increasing and decreasing values of F_{surf} (direction indicated by arrows) spanning the range simulated in WAIS 1080. The forward and reverse pathways are offset to aid visualization. Text inset identifies solutions associated with $\kappa_{\text{P}} = \kappa_{\text{conv}}$ (“convective steady states”) and $\kappa_{\text{P}} = \kappa_{\text{diff}}$ (“diffusive steady states”). (b-e) Plots showing equilibrated h (b,d) and Δb (c,e) values associated with diffusive steady states (b,c) and convective steady states (d,e) for a range of Ψ_{in} and F_{surf} forcing values. Regions of each phase space left white do not support steady states with the relevant κ_{P} value. Magenta contours outline the parameter space able to support both diffusive and convective steady states. The white star in (b) shows the time mean WAIS 1080 forcing. Convective steady states to with $h > 700$ m (depth of the water column) are not physical, but are shown here since transient forcing in this region is permissible.

238 plied. These bistable states have comparable mCDW depths to the observed warm and
 239 cool phases (Figure 1d), although available observations of cool phases are stably strat-
 240 ified (Webber et al., 2017; Yang et al., 2022) .

241 Bistability occurs over a large portion of the explored forcing space (magenta con-
 242 tour, Figure 3b-e), which spans realistic ranges of F_{surf} and Ψ_{in} (monthly mean values
 243 span -1.7×10^{-7} to 0.5×10^{-7} $\text{m}^2 \text{s}^{-3}$ and 0 to 0.3 Sv in WAIS 1080). Forcing com-
 244 binations that support only one steady state solution are referred to as monostable. Fig-
 245 ure 3b-e suggests variations in both F_{surf} (vertical paths in Figure 3b-e) and Ψ_{in} (hor-
 246 izontal paths) can generate hysteresis by shifting the system from one monostable re-
 247 gion to the other via the bistable region. Whilst Figure 3 displays numerically equilibrated
 248 model output, a benefit of this model’s simplicity is that it permits analytical solutions
 249 for end member cases and easy exploration of parameter space (Supporting Information
 250 S3). Overall, model behavior is not qualitatively sensitive to reasonable parameter per-
 251 turbations; a summary of our sensitivity assessment appears in Table S1.

252 3.2 Transient model behavior

253 The presence of bistability in this simple model poses an alternate explanation for
 254 the decadal scale ~ 400 m thermocline depth variations observed at the Dotson Ice Front.
 255 The observed variability could, as previously implied, be a low frequency response to low
 256 frequency variations in the supply of mCDW to the ice front. Alternatively, our simple
 257 model suggests that transient perturbations of either mCDW supply or coastal surface
 258 buoyancy fluxes could trigger transitions between self-reinforcing deep and shallow ther-
 259 mocline states, perhaps explaining the large amplitude and persistent nature of the ob-
 260 served cool and warm phases. This possibility is tested with transiently forced exper-
 261 iments.

262 The ice front overturning model is initialized with either weak or strong stratifi-
 263 cation and forced with WAIS 1080 climatological mean F_{surf} and Ψ_{in} values until an-
 264 nual patterns of ice front stratification (Δb) and thermocline depth (h) equilibrate. The
 265 WAIS 1080 climatology lies sufficiently within the bistable forcing region (yellow shad-
 266 ing, Figure 4a,b) to support temporally varying solutions that persist in their initial regime.
 267 These equilibrated simulations are then transiently forced with perturbed climatologies
 268 to prompt regime transitions that persist when the forcing returns to the original pat-
 269 tern. Two winter perturbations are constructed by decreasing the May-September F_{surf}
 270 or Ψ_{in} forcing by a constant offset, and two summer perturbations are constructed by
 271 increasing the December-April F_{surf} or Ψ_{in} forcing by a constant offset. Winter and sum-
 272 mer perturbations are then tested for their ability to drive transitions from the diffusive
 273 to the convective regime and vice versa. Seasonal perturbations are chosen based on the
 274 strong seasonality of F_{surf} ; we also use a seasonal perturbation for Ψ_{in} experiments for
 275 consistency, although Ψ_{in} has a more complex annual pattern (Figure 4b inset).

276 Figure 4a,b show the smallest amplitude winter and summer offsets that trigger
 277 regime shifts within two consecutive years of perturbed forcing. When regime transitions
 278 are simulated (Figure 4c,e,f), lags between the thermocline response and stratification
 279 response align with observations. In agreement with the observed transition from a warm
 280 phase to a cool phase between 2009 and 2012 (Figure 1d), thermocline depth anomalies
 281 lag buoyancy anomalies during modeled transitions to convective conditions (Figure 4c).
 282 The shoaled thermocline observed in 2018 may represent a transition to warm phase con-
 283 ditions with the opposite lag, thermocline shoaling preceding stratification strengthen-
 284 ing. If so, the simulated lags between thermocline depth anomalies and buoyancy anom-
 285 alies in both Ψ_{in} and F_{surf} -driven transitions to diffusive conditions (Figure 4d,e) are also
 286 consistent with observations.

287 In addition to capturing the nature of observed transitions between warm and cool
 288 phases at the Dotson Ice Front, our idealized model anticipates the shallow bias and di-

289 minished variability of the ice front thermocline depth in WAIS 1080 (0°C isotherm depth
 290 ranges from 440-820 m in observations and only 255-420 m in WAIS 1080). When the
 291 ice front overturning model is forced with the full WAIS 1080 1992-2019 timeseries of
 292 F_{surf} and Ψ_{in} , rather than climatological values, simulations initialized with convective
 293 conditions rapidly transition to diffusive conditions and remain there (Figure S5), con-
 294 sistent with WAIS 1080 failing to capture convective events. In general, transitions to
 295 convective states required larger deviations from the WAIS 1080 forcing than transitions
 296 to diffusive states. Significantly stronger negative F_{surf} values than those simulated in
 297 WAIS 1080 were needed to generate a regime shift within a single year (minimum win-
 298 ter values of $-3 \times 10^{-7} \text{ m}^2 \text{ s}^{-3}$ compared to minimum WAIS 1080 forcing of $-1.7 \times$
 299 $10^{-7} \text{ m}^2 \text{ s}^{-3}$), thus our choice to present results of two-year perturbations in Figure 4.
 300 ERA5 has been shown to underestimate near-surface wind speeds along the Antarctic
 301 coastline (Caton Harrison et al., 2022) and this may induce an underestimation of win-
 302 ter F_{surf} minima in WAIS 1080, alternatively, WAIS 1080 and our idealized model may
 303 exaggerate the barrier to convection. Observational estimates indicate gross annual ASP
 304 sea-ice formation varies significantly, ranging from 139 km^3 to 80 km^3 from 2017 to 2020
 305 (Macdonald et al., 2023), suggesting the large interannual variations in surface buoyancy
 306 forcing needed to trigger regime shifts in our model are plausible.

307 Reductions in Ψ_{in} , whether transient (Figure 4d) or more sustained (Figure S6),
 308 do not trigger transitions to convective conditions for any physical choice of offset (en-
 309 forcing $\Psi_{\text{in}} > 0$). Such regime shifts are not supported as reducing Ψ_{in} initially strength-
 310 ens ice front stratification in our simulations. This anticorrelation between thermocline
 311 depth and stratification when Ψ_{in} is reduced is not supported by observations or WAIS
 312 1080, however, and may reflect the simplicity of our model. These experiments affirm
 313 the possibility that polynya forcing can drive realistic transitions to cool phases, but do
 314 not negate the possibility that variable mCDW supply could also drive such transitions.
 315 Both forcings appear able to drive realistic transitions to warm conditions.

316 4 Discussion and Outlook

317 This study intentionally targets a simplified representation of West Antarctic coastal
 318 ocean dynamics to highlight mechanistic links between surface forcing, interior mixing,
 319 thermocline depth variations, and overturning pathways on the West Antarctic conti-
 320 nental shelf. The key result is the identification of positive feedbacks that are indepen-
 321 dent of the supply of mCDW from the continental shelf break. These feedbacks involve
 322 interactions between basal ice shelf melt rates and thermocline stratification strength at
 323 the ice shelf front and provide a plausible explanation for the amplitude and duration
 324 of multi-year warm and cool phases observed, for example, at the Dotson Ice Front. The
 325 modeled thermocline variability tracks the strength of convection in the adjacent coastal
 326 polynya and successfully reproduces observed stratification changes, not previously iden-
 327 tified, associated with transitions between the warm and cool phases. The importance
 328 of coastal convection to this feedback highlights the need to appropriately represent ver-
 329 tical mixing when simulating West Antarctic ocean-forced ice shelf melt. Modeled shifts
 330 in convection strength can be triggered by both variable mCDW supply from the con-
 331 tinental shelf break (a remote forcing), and variable surface buoyancy fluxes within the
 332 polynya (a local forcing). Since future trends in mCDW supply from the shelf-break and
 333 sea-ice production in coastal polynyas may not align, understanding the relative impor-
 334 tance of these forcings is important for projecting future melt. Finally, given the pos-
 335 itive feedback identified cannot be represented in ocean models that apply fixed melt-
 336 water inputs, our results emphasize that future work should utilize models that simu-
 337 late basal melt within cavities. As a first step on this path, we show that the idealized
 338 model predicts the shallow, steady bias of the Dotson Ice Front thermocline in the WAIS
 339 1080 model based on its forcing, demonstrating the power of using idealized models to
 340 interpret biases in complex models.

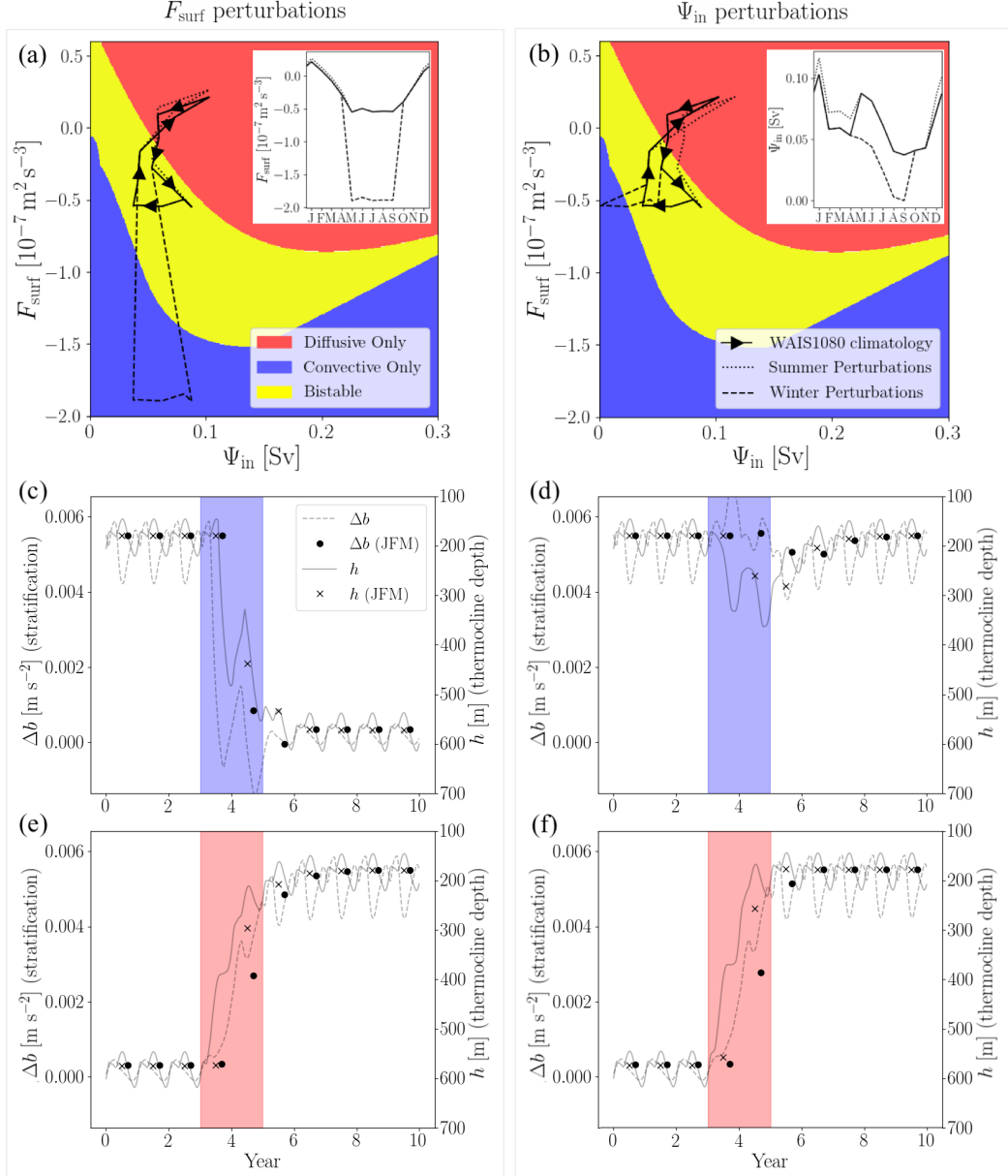


Figure 4. (a, b) The forcing parameter space partitioned into regions supporting only one steady state solution (diffusive in red; convective in blue) and both solutions (bistability in yellow). Climatological mean F_{surf} and Ψ_{in} values from the WAIS 1080 simulation are shown within this forcing space (solid black lines) with arrows indicating the progression of an annual cycle. Winter perturbed forcings (dashed lines) and summer perturbed forcings (dotted lines) are indicated within the forcing space for F_{surf} experiments (a) and Ψ_{in} experiments (b). Forcing climatologies are shown as a function of time in inset panels for clarity. (c-f) Full time series of h (solid grey lines) and Δb (dashed grey lines) alongside January-March mean values (black crosses and circles, respectively) from transient forcing experiments described in the main text. Shaded regions indicate the perturbation period (years 4 and 5) and whether a winter (blue; c,d) or summer (red; e,f) perturbation was prescribed.

341 The idealized representation of coastal dynamics in this study neglects certain pro-
 342 cesses that merit discussion. The most notable simplification is that WW, meltwater mod-
 343 ified CDW, and other surface waters are combined in a single box. As a result, the spa-
 344 tial structure of glacial meltwater plumes exiting the cavity (e.g. Garabato et al., 2017;
 345 Zheng et al., 2021) and exiting the model domain are omitted, and buoyancy from melt-
 346 water is uniformly distributed above the thermocline. This simplification may lead to
 347 spurious stratification strengthening in response to reductions in mCDW supply (Fig-
 348 ure 4d), as unresolved structures may remove meltwaters from the ice shelf front more
 349 rapidly than our model suggests. The truncated vertical structure of our model also leads
 350 to unrealistic year-round convection during cool phases in transiently forced simulations
 351 (Figure 4). In the real ocean, positive F_{surf} forcing during summer months may halt con-
 352 vection by stratifying a small fraction of the upper water column whilst leaving the deep
 353 thermocline position intact. In our model, positive buoyancy fluxes are distributed over
 354 the full thermocline depth, presenting an exaggerated barrier to restratification. Con-
 355 sequently, the water column convects year-round rather than being preconditioned for
 356 the annual recurrence of convection. Another noteworthy simplification is that, since Ψ_{in}
 357 and F_{surf} are prescribed, we neglect feedbacks that influence their magnitude. Shoreward
 358 mCDW transport in the Amundsen Sea may decrease (Moorman et al., 2020; Beadling
 359 et al., 2022) or increase (Si et al., 2023) in response to coastal freshening, and coastal
 360 sea-ice formation rates may likewise be sensitive to coastal freshening by meltwater. Fi-
 361 nally, we note that this model does not represent advection of non-local meltwater to the
 362 ice front (e.g. by the Antarctic Coastal Current Flexas et al., 2022). The ability for our
 363 idealized model to capture key features of observed Amundsen Sea mCDW variability
 364 despite these simplifications speaks to the importance of ice front thermocline stratifi-
 365 cation strength to ocean-driven glacial melt variability on decadal timescales.

366 This work builds on regional modeling (St-Laurent et al., 2015; Caillet et al., 2022;
 367 Bett et al., 2020; Naughten et al., 2022), idealized modeling (Petty et al., 2013; Silvano
 368 et al., 2018), and observational evidence (Webber et al., 2017) indicating coastal buoy-
 369 ancy forcing can modulate ocean heat availability at West Antarctic ice shelves. At the
 370 Pine Island Ice Front, anomalously strong coastal surface buoyancy fluxes can explain
 371 the cool period observed from 2011 to 2013 in regional models and observations (St-Laurent
 372 et al., 2015; Webber et al., 2017). At longer timescales, simulated transitions between
 373 cool and warm Amundsen shelf states closely track surface buoyancy forcing changes (Caillet
 374 et al., 2022). For the Dotson Ice Shelf, Caillet et al. (2022) simulate persistent low or
 375 high melt rates in response to strong negative and positive perturbations to surface buoy-
 376 ancy forcing, respectively, and large decadal variations in melt rates for intermediate sur-
 377 face buoyancy forcing perturbations, consistent with the bistability mechanism presented
 378 here (see Figure 5 in Caillet et al., 2022). Idealized models have primarily been used to
 379 assess the Amundsen Sea mean state, with bulk mixed layer models indicating a lead-
 380 ing role for buoyancy fluxes in setting the shallow winter mixed layer depths typical of
 381 the West Antarctic shelf relative to other Antarctic regions (Petty et al., 2013; Silvano
 382 et al., 2018). Whilst Amundsen Sea variability at interannual and longer timescales has
 383 not been targeted with idealized models, there is precedent elsewhere. For example, con-
 384 ceptual models have been used to interrogate bistable low and high melt states of the
 385 Filchner-Ronne Ice Shelf enabled by coastal buoyancy feedbacks analogous to those iden-
 386 tified here (Hazel & Stewart, 2020). Our approach incorporates the consideration of buoy-
 387 ancy central to these results into a “thermocline model” framework based on closing wa-
 388 termass transformation pathways, a framework originally applied to the global overturn-
 389 ing circulation (e.g. Gnanadesikan, 1999; Marshall & Zanna, 2014; Thompson et al., 2019).

390 We take away two important lessons for future studies of warm West Antarctic shelf
 391 seas. Firstly, the dynamics that govern the exposure of ice shelves to ocean heat must
 392 account not only for variability in mCDW supply, but also mCDW consumption or trans-
 393 formation, with the latter having received significantly less attention. Secondly, we can-
 394 not neglect the dynamical effects of meltwater in a salinity stratified system; ongoing ob-

servational monitoring and accurate simulation of ice front stratification strength should
be prioritized.

Open Research Section

Data and code required to reproduce all figures in the main text and Supporting Information provided at <https://doi.org/10.5281/zenodo.7987113>. A binder environment (see <https://mybinder.org/> for details) has been constructed so that readers can open, edit, and execute all code from a browser (click “launch binder” button on the GitHub repository home page linked to the listed doi). Editing within the binder environment will not alter the original file, so readers should feel free to manipulate provided code.

Acknowledgments

RM acknowledges the support of the General Sir John Monash Foundation. AT acknowledges support from NSF grants OPP-1644172 and OCE-2023259. EW acknowledges support from Caltech’s Terrestrial Hazard Observations and Reporting Center. We thank Michael Schodlock and Mar Flexas for their assistance in accessing and utilizing WAIS 1080 output. We thank Channing Prend and Ryan Eusebi for their helpful comments on the initial manuscript. We also thank Kevin Speer and Alessandro Silvano for helpful conversations. Finally, we acknowledge valuable work performed in the collection, collation and open access publishing of shipborne observational data by the Marine Geoscience Data System (MGDS), the Korean Polar Data Center (KPDC), and the authors of Jenkins et al. (2018).

References

- Adusumilli, S., Fricker, H. A., Medley, B., Padman, L., & Siegfried, M. R. (2020). Interannual variations in meltwater input to the southern ocean from antarctic ice shelves. *Nature geoscience*, *13*(9), 616–620.
- Assmann, K. M., Jenkins, A., Shoosmith, D. R., Walker, D. P., Jacobs, S. S., & Nicholls, K. W. (2013). Variability of circumpolar deep water transport onto the Amundsen Sea Continental shelf through a shelf break trough. *Journal of Geophysical Research: Oceans*, *118*(12), 6603–6620. doi: 10.1002/2013JC008871
- Beadling, R., Krasting, J., Griffies, S., Hurlin, W., Bronselaer, B., Russell, J., ... Winton, M. (2022). Importance of the antarctic slope current in the southern ocean response to ice sheet melt and wind stress change. *Journal of Geophysical Research: Oceans*, *127*(5), e2021JC017608.
- Bett, D. T., Holland, P. R., Naveira Garabato, A. C., Jenkins, A., Dutrieux, P., Kimura, S., & Fleming, A. (2020, sep). The Impact of the Amundsen Sea Freshwater Balance on Ocean Melting of the West Antarctic Ice Sheet. *Journal of Geophysical Research: Oceans*, *125*(9), e2020JC016305. doi: 10.1029/2020JC016305
- Boot, D., Van Westen, R. M., & Dijkstra, H. A. (2021, feb). Multidecadal polynya formation in a conceptual (box) model. *Ocean Science*, *17*(1), 335–350. doi: 10.5194/os-17-335-2021
- Caillet, J., Jourdain, N. C., Mathiot, P., Hellmer, H. H., & Mougnot, J. (2022). Drivers and reversibility of abrupt ocean state transitions in the amundsen sea, antarctica. *Journal of Geophysical Research: Oceans*, e2022JC018929.
- Caton Harrison, T., Biri, S., Bracegirdle, T. J., King, J. C., Kent, E. C., Vignon, É., & Turner, J. (2022). Reanalysis representation of low-level winds in the antarctic near-coastal region. *Weather and Climate Dynamics*, *3*(4), 1415–1437.
- Dotto, T. S., Garabato, A. C., Bacon, S., Holland, P. R., Kimura, S., Firing, Y. L.,

- 444 ... Jenkins, A. (2019). Wind-driven processes controlling oceanic heat delivery
 445 to the amundsen sea, antarctica. *Journal of Physical Oceanography*, 49(11),
 446 2829–2849. doi: 10.1175/JPO-D-19-0064.1
- 447 Dotto, T. S., Garabato, A. C. N., Wåhlin, A. K., Bacon, S., Holland, P. R., Kimura,
 448 S., ... Jenkins, A. (2020). Control of the Oceanic Heat Content of the Getz-
 449 Dotson Trough, Antarctica, by the Amundsen Sea Low. *Journal of Geophysical*
 450 *Research: Oceans*, 125(8), e2020JC016113. doi: 10.1029/2020JC016113
- 451 Dutrieux, P., De Rydt, J., Jenkins, A., Holland, P. R., Ha, H. K., Lee, S. H., ...
 452 Schröder, M. (2014). Strong sensitivity of Pine Island ice-shelf melting to cli-
 453 matic variability. *Science*, 343(6167), 174–178. doi: 10.1126/science.1244341
- 454 Fetterer, F., & Stewart., J. S. (2020). *U.S. National Ice Center Arctic and Antarc-*
 455 *tic Sea Ice Concentration and Climatologies in Gridded Format, Version 1*. Na-
 456 tional Snow and Ice Data Center. Retrieved from [https://nsidc.org/data/](https://nsidc.org/data/g10033/versions/1)
 457 [g10033/versions/1](https://nsidc.org/data/g10033/versions/1) doi: 10.7265/46cc-3952
- 458 Flexas, M. M., Thompson, A. F., Schodlok, M. P., Zhang, H., & Speer, K. (2022).
 459 Antarctic peninsula warming triggers enhanced basal melt rates throughout
 460 west antarctica. *Science Advances*, 8(31), eabj9134.
- 461 Fürst, J. J., Durand, G., Gillet-Chaulet, F., Tavard, L., Rankl, M., Braun, M., &
 462 Gagliardini, O. (2016). The safety band of Antarctic ice shelves. *Nature*
 463 *Climate Change*, 6(5), 479–482. doi: 10.1038/NCLIMATE2912
- 464 Garabato, A. C. N., Forryan, A., Dutrieux, P., Brannigan, L., Biddle, L. C., Hey-
 465 wood, K. J., ... Kimura, S. (2017). Vigorous lateral export of the meltwater
 466 outflow from beneath an antarctic ice shelf. *Nature*, 542(7640), 219–222.
- 467 Gnanadesikan, A. (1999). A simple predictive model for the structure of the oceanic
 468 pycnocline. *Science*, 283(5410), 2077–2079. doi: 10.1126/science.283.5410
 469 .2077
- 470 Hazel, J. E., & Stewart, A. L. (2020, apr). Bistability of the Filchner-Ronne Ice
 471 Shelf Cavity Circulation and Basal Melt. *Journal of Geophysical Research:*
 472 *Oceans*, 125(4), e2019JC015848. doi: 10.1029/2019JC015848
- 473 Hersbach, H., Bell, B., Berrisford, P., Hirahara, S., Horányi, A., Muñoz-Sabater, J.,
 474 ... others (2020). The era5 global reanalysis. *Quarterly Journal of the Royal*
 475 *Meteorological Society*, 146(730), 1999–2049.
- 476 Holland, P. R., Bracegirdle, T. J., Dutrieux, P., Jenkins, A., & Steig, E. J.
 477 (2019). West Antarctic ice loss influenced by internal climate variabil-
 478 ity and anthropogenic forcing. *Nature Geoscience*, 12(9), 718–724. doi:
 479 10.1038/s41561-019-0420-9
- 480 IMBIE Team. (2018). Mass balance of the Antarctic Ice Sheet from 1992 to 2017.
 481 *Nature* 2018 558:7709, 558(7709), 219–222. doi: 10.1038/s41586-018-0179-y
- 482 Jenkins, A., Dutrieux, P., Jacobs, S., Steig, E. J., Gudmundsson, G. H., Smith, J.,
 483 & Heywood, K. J. (2016). Decadal Ocean Forcing and Antarctic Ice Sheet
 484 Response: LESSONS FROM THE AMUNDSEN SEA. *Oceanography*, 29(4),
 485 106–117.
- 486 Jenkins, A., Shoosmith, D., Dutrieux, P., Jacobs, S., Kim, T. W., Lee, S. H., ...
 487 Stammerjohn, S. (2018). West Antarctic Ice Sheet retreat in the Amundsen
 488 Sea driven by decadal oceanic variability. *Nature Geoscience*, 11(10), 733–738.
 489 doi: 10.1038/s41561-018-0207-4
- 490 Kim, T. W., Ha, H. K., Wåhlin, A. K., Lee, S. H., Kim, C. S., Lee, J. H., & Cho,
 491 Y. K. (2017, jan). Is Ekman pumping responsible for the seasonal variation
 492 of warm circumpolar deep water in the Amundsen Sea? *Continental Shelf*
 493 *Research*, 132, 38–48. doi: 10.1016/j.csr.2016.09.005
- 494 Kim, T.-W., Yang, H. W., Dutrieux, P., Wåhlin, A. K., Jenkins, A., Kim, Y. G., ...
 495 Cho, Y.-K. (2021). Interannual Variation of Modified Circumpolar Deep Water
 496 in the Dotson-Getz Trough, West Antarctica. *Journal of Geophysical Research:*
 497 *Oceans*, 126(12), e2021JC017491.
- 498 Macdonald, G. J., Ackley, S. F., Mestas-Nuñez, A. M., & Blanco-Cabanillas, A.

- 499 (2023). Evolution of the dynamics, area, and ice production of the amundsen
500 sea polynya, antarctica, 2016–2021. *The Cryosphere*, *17*(2), 457–476.
- 501 Marshall, D. P., & Zanna, L. (2014). A conceptual model of ocean heat uptake un-
502 der climate change. *Journal of Climate*, *27*(22), 8444–8465.
- 503 Martinson, D. G., Killworth, P. D., & Gordon, A. L. (1981). A convective model for
504 the weddell polynya. *Journal of Physical Oceanography*, *11*(4), 466–488.
- 505 McDougall, T. J., & Dewar, W. K. (1998). Vertical mixing and cabbeling in layered
506 models. *Journal of Physical Oceanography*, *28*(7), 1458–1480.
- 507 Moorman, R., Morrison, A. K., & McC. Hogg, A. (2020). Thermal responses to
508 antarctic ice shelf melt in an eddy-rich global ocean–sea ice model. *Journal of*
509 *Climate*, *33*(15), 6599–6620.
- 510 Morlighem, M., Rignot, E., Binder, T., Blankenship, D., Drews, R., Eagles, G., ...
511 Young, D. A. (2020). Deep glacial troughs and stabilizing ridges unveiled
512 beneath the margins of the Antarctic ice sheet. *Nature Geoscience*, *13*(2),
513 132–137. doi: 10.1038/s41561-019-0510-8
- 514 Mouginot, J., Rignot, E., & Scheuchl, B. (2014). Sustained increase in ice discharge
515 from the amundsen sea embayment, west antarctica, from 1973 to 2013. *Geo-*
516 *physical Research Letters*, *41*(5), 1576–1584.
- 517 Munk, W. H. (1966). Abyssal recipes. In *Deep sea research and oceanographic ab-*
518 *stracts* (Vol. 13, pp. 707–730).
- 519 Naughten, K. A., Holland, P. R., Dutrieux, P., Kimura, S., Bett, D. T., & Jenkins,
520 A. (2022). Simulated twentieth-century ocean warming in the amundsen sea,
521 west antarctica. *Geophysical Research Letters*, *49*(5), e2021GL094566.
- 522 Paolo, F. S., Fricker, H. A., & Padman, L. (2015). Volume loss from antarctic ice
523 shelves is accelerating. *Science*, *348*(6232), 327–331. doi: 10.1126/science
524 .aaa0940
- 525 Petty, A. A., Feltham, D. L., & Holland, P. R. (2013). Impact of atmospheric forc-
526 ing on antarctic continental shelf water masses. *Journal of Physical Oceanogra-*
527 *phy*, *43*(5), 920–940.
- 528 Pritchard, H., Ligtenberg, S. R., Fricker, H. A., Vaughan, D. G., van den Broeke,
529 M. R., & Padman, L. (2012). Antarctic ice-sheet loss driven by basal melting
530 of ice shelves. *Nature*, *484*(7395), 502–505.
- 531 Schmidtko, S., Heywood, K. J., Thompson, A. F., & Aoki, S. (2014). Multidecadal
532 warming of antarctic waters. *Science*, *346*(6214), 1227–1231.
- 533 Shepherd, A., Wingham, D., & Rignot, E. (2004). Warm ocean is eroding west
534 antarctic ice sheet. *Geophysical Research Letters*, *31*(23).
- 535 Si, Y., Stewart, A. L., & Eisenman, I. (2023). Heat transport across the antarctic
536 slope front controlled by cross-slope salinity gradients. *Science Advances*,
537 *9*(18), eadd7049.
- 538 Silvano, A., Holland, P. R., Naughten, K. A., Dragomir, O., Dutrieux, P., Jenkins,
539 A., ... others (2022). Baroclinic ocean response to climate forcing regu-
540 lates decadal variability of ice-shelf melting in the amundsen sea. *Geophysical*
541 *Research Letters*, *49*(24), e2022GL100646.
- 542 Silvano, A., Rintoul, S. R., Peña-Molino, B., Hobbs, W. R., Van Wijk, E., Aoki, S.,
543 ... Williams, G. D. (2018, apr). Freshening by glacial meltwater enhances
544 melting of ice shelves and reduces formation of Antarctic Bottom Water. *Sci-*
545 *ence Advances*, *4*(4), eaap9467. doi: 10.1126/sciadv.aap9467
- 546 St-Laurent, P., Klinck, J. M., & Dinniman, M. S. (2015). Impact of local winter
547 cooling on the melt of Pine Island Glacier, Antarctica. *Journal of Geophysical*
548 *Research: Oceans*, *120*(10), 6718–6732. doi: 10.1002/2015JC010709
- 549 Tamura, T., Ohshima, K. I., Fraser, A. D., & Williams, G. D. (2016, may). Sea
550 ice production variability in Antarctic coastal polynyas. *Journal of Geophysical*
551 *Research: Oceans*, *121*(5), 2967–2979. doi: 10.1002/2015JC011537
- 552 Tamura, T., Ohshima, K. I., & Nihashi, S. (2008). Mapping of sea ice production for
553 antarctic coastal polynyas. *Geophysical Research Letters*, *35*(7).

- 554 Thompson, A. F., Hines, S. K., & Adkins, J. F. (2019). A southern ocean mech-
555 anism for the interhemispheric coupling and phasing of the bipolar seesaw.
556 *Journal of Climate*, *32*(14), 4347–4365.
- 557 Turner, J., Orr, A., Gudmundsson, G. H., Jenkins, A., Bingham, R. G., Hillenbrand,
558 C.-D., & Bracegirdle, T. J. (2017). Atmosphere-ocean-ice interactions in the
559 amundsen sea embayment, west antarctica. *Reviews of Geophysics*, *55*(1),
560 235–276.
- 561 Wåhlin, A. K., Steiger, N., Darelius, E., Assmann, K. M., Glessmer, M. S., Ha,
562 H. K., ... Viboud, S. (2020). Ice front blocking of ocean heat trans-
563 port to an Antarctic ice shelf. *Nature*, *578*(7796), 568–571. doi: 10.1038/
564 s41586-020-2014-5
- 565 Walin, G. (1982). On the relation between sea-surface heat flow and thermal circula-
566 tion in the ocean. *Tellus*, *34*(2), 187–195.
- 567 Walker, D. P., Brandon, M. A., Jenkins, A., Allen, J. T., Dowdeswell, J. A., &
568 Evans, J. (2007). Oceanic heat transport onto the Amundsen Sea shelf
569 through a submarine glacial trough. *Geophysical Research Letters*, *34*(2).
570 doi: 10.1029/2006GL028154
- 571 Webber, B. G., Heywood, K. J., Stevens, D. P., & Assmann, K. M. (2019). The
572 impact of overturning and horizontal circulation in pine Island trough on ice
573 shelf melt in the eastern Amundsen Sea. *Journal of Physical Oceanography*,
574 *49*(1), 63–83. doi: 10.1175/JPO-D-17-0213.1
- 575 Webber, B. G., Heywood, K. J., Stevens, D. P., Dutrieux, P., Abrahamsen, E. P.,
576 Jenkins, A., ... Kim, T. W. (2017). Mechanisms driving variability in the
577 ocean forcing of Pine Island Glacier. *Nature Communications*, *8*(1), 1–8. doi:
578 10.1038/ncomms14507
- 579 Yang, H. W., Kim, T.-W., Dutrieux, P., Wåhlin, A., Jenkins, A., Ha, H. K., ... oth-
580 ers (2022). Seasonal variability of ocean circulation near the dotson ice shelf,
581 antarctica. *Nature communications*, *13*(1), 1138.
- 582 Zheng, Y., Heywood, K. J., Webber, B. G., Stevens, D. P., Biddle, L. C., Boehme,
583 L., & Loose, B. (2021). Winter seal-based observations reveal glacial melt-
584 water surfacing in the southeastern amundsen sea. *Communications Earth &*
585 *Environment*, *2*(1), 40.